Chem

Article

Interfacial hydrogen-bond network regulation enables selective CO_2 reduction to ethanol on copper-free electrocatalysts

Graphical abstract

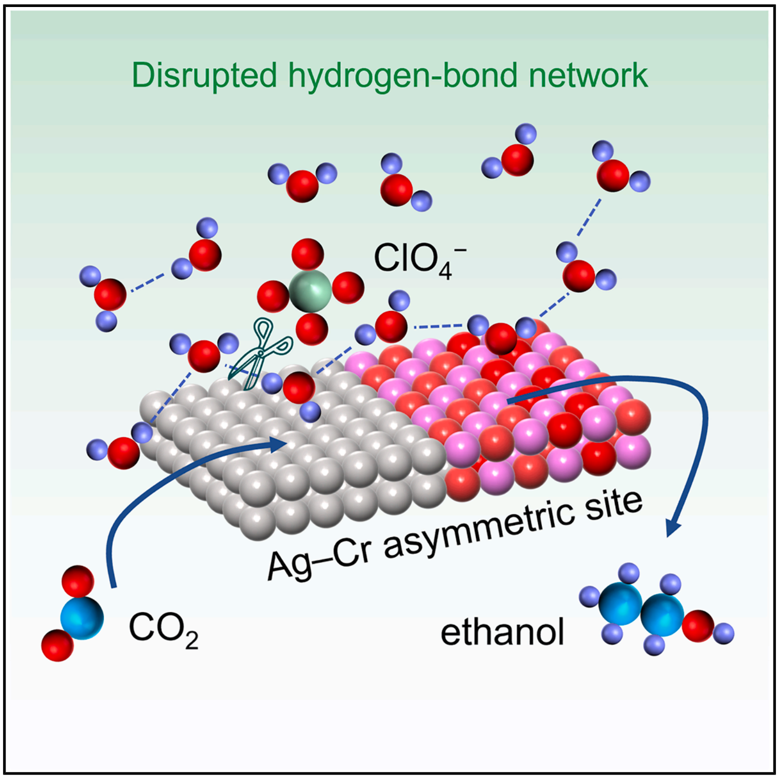

Highlights

- Copper-free Ag/Cr_2O_3 electrocatalyst selectively reduces CO_2 to ethanol
- Perchlorate anions disrupt the hydrogen-bond networks and promote C–C coupling
- The ethanol yields of various anions follow the Hofmeister series trend
- >50% faradaic efficiency for ethanol at ∼160 mA/cm^2 in a flow cell

Authors

Shuxia Liu, Jixian Hu, Jiarui Liu, ...,
Yinghe Zhao, Qing Li, Tanyuan Wang

Correspondence

qing_li@hust.edu.cn (Q.L.),
wangty@hust.edu.cn (T.W.)

In brief

Selective electroreduction of CO_2 into ethanol—a storable fuel—has been limited almost exclusively to copper. Herein, a copper-free Ag/Cr_2O_3 catalyst is designed to produce ethanol with >50% faradaic efficiency at ∼160 mA/cm^2 with the assistance of perchlorate. The presence of perchlorate disrupts the continuous hydrogen-bond network, thereby inhibiting the competing hydrogen evolution. The Ag–Cr asymmetric sites further stabilize the C–C coupling intermediates and lower the ethanol pathway barriers over ethylene, thus enabling selective ethanol generation.

Liu et al., 2026, Chem *12*, 103078
November 12, 2026 © 2026 Elsevier Inc. All rights are reserved, including those for text and data mining, AI training, and similar technologies.
https://doi.org/10.1016/j.chempr.2026.103078

CellPress

Please cite this article in press as: Liu et al., Interfacial hydrogen-bond network regulation enables selective CO_2 reduction to ethanol on copper-free electrocatalysts, Chem (2026), https://doi.org/10.1016/j.chempr.2026.103078

Chem

CellPress

Article

Interfacial hydrogen-bond network regulation enables selective CO_2 reduction to ethanol on copper-free electrocatalysts

Shuxia Liu,[1,4] Jixian Hu,[1,4] Jiarui Liu,[1] Zijie Lin,[1] Shuo Wang,[2] Hao Sun,[2] Yinghe Zhao,[3] Qing Li,[1,5,*] and Tanyuan Wang[1,*]

[1]State Key Laboratory of Material Processing and Die & Mould Technology, School of Materials Science and Engineering, Huazhong University of Science and Technology, Wuhan 430074, Hubei, China

[2]Frontiers Science Center for Transformative Molecules, School of Chemistry and Chemical Engineering, Zhangjiang Institute for Advanced Study, Shanghai Jiao Tong University, Shanghai 200240, China

[3]School of Physical Science and Technology, Inner Mongolia University, Hohhot 010021, Inner Mongolia, China

[4]These authors contributed equally

[5]Lead contact

*Correspondence: qing_li@hust.edu.cn (Q.L.), wangty@hust.edu.cn (T.W.)

https://doi.org/10.1016/j.chempr.2026.103078

THE BIGGER PICTURE Electrochemical CO_2 reduction powered by renewable electricity offers a promising route to close the carbon cycle and produce valuable chemicals. Among the possible products, ethanol is especially attractive because of its high energy density and compatibility with the existing fuel infrastructure. However, the selective electrosynthesis of ethanol from CO_2 remains challenging, and the catalysts are almost exclusively limited to copper—a material with a complex product distribution during CO_2 reduction. It is of great significance to design a new electrocatalytic interface that can selectively convert CO_2 into ethanol without side reactions.

This work presents a strategy based on anion regulation at the electrode/electrolyte interface to achieve 100% ethanol selectivity over ethylene (the main byproduct for C–C coupling in electrochemical CO_2 reduction) on a copper-free Ag/Cr_2O_3 heterostructure for CO_2 reduction. The effect of Hofmeister series anions (ranked by their water-withdrawing effect for proteins) on the interfacial water structures during CO_2 reduction is revealed, with perchlorate found to be the most efficient anion to suppress hydrogen evolution and promote CO_2 reduction. The benefits of asymmetric Ag–Cr active sites for selective ethanol generation during CO_2 reduction via asymmetric hydrogenation are also illustrated. Based on the above research, a guideline on the design of an ethanol-selective, copper-free interface for electrochemical CO_2 reduction can be established, which involves the combination of asymmetric sites that can activate CO_2 and anions that can inhibit hydrogen evolution. This work can provide valuable insights for the future design of selective C–C coupling catalysts/interfaces that can achieve the efficient utilization of carbon dioxide and can further contribute to the building of a sustainable society.

SUMMARY

Developing a Cu-free electrocatalytic system for CO_2 reduction toward a multi-carbon product remains challenging due to the limited understanding of C–C coupling. Herein, an Ag/Cr_2O_3 heterostructure is reported to achieve selective ethanol electrosynthesis from CO_2 with anions to modulate the electrocatalytic interfaces. The performance of Ag/Cr_2O_3 follows the trend of $ClO_4^- > NO_3^- > NO_2^- > HCO_3^-/HPO_4^{2-}/SO_4^{2-}$ for different anions, which is similar to the tendency of Hofmeister anions to disrupt water's structure. Notably, Ag/Cr_2O_3 exhibits a faradaic efficiency $(FE)_{ethanol}$ of 51.8% with a stable response at ~160 mA cm^{-2} in a flow cell containing ClO_4^-. *In situ* characterizations and theoretical calculations demonstrate that ClO_4^- reduces the number of interfacial hydrogen bonds, thus inhibiting hydrogen evolution. While the Ag-Cr asymmetric sites stabilize the C–C coupling intermediates and favor the ethanol pathway over ethylene, this enables selective ethanol generation. This work extends the approach for multi-carbon generation from CO_2.

© 2026 Elsevier Inc.
All rights are reserved, including those for text and data mining, AI training, and similar technologies.

Please cite this article in press as: Liu et al., Interfacial hydrogen-bond network regulation enables selective CO_2 reduction to ethanol on copper-free electrocatalysts, Chem (2026), https://doi.org/10.1016/j.chempr.2026.103078

INTRODUCTION

The electrochemical CO_2 reduction reaction (CO_2RR) has been established as a pivotal strategy for transforming CO_2 into value-added products, and it is increasingly regarded as a sustainable pathway toward closing the carbon cycle and mitigating climate change.[1,2] Among the CO_2RR-derived species, ethanol has been identified as a particularly attractive product owing to its high energy density (–1,366.8 kJ mol^{-1}) and favorable characteristics for storage and transportation.[3–5] Currently, most of the catalysts identified for ethanol production in CO_2RR are based on copper.[6,7] However, thermodynamic constraints give rise to the formation of competing hydrocarbon (e.g., ethylene) byproducts on Cu-based catalysts, which significantly impedes the selective electrosynthesis of ethanol from CO_2.[8]

*CO is the commonly reported key intermediate that effectively facilitates C–C coupling for ethanol production. Therefore, non-copper materials that can effectively generate or adsorb *CO may potentially demonstrate an efficient CO_2RR catalytic performance for ethanol generation. Recently, non-copper materials such as NiO,[5] Fe porphyrinic-based metal-organic frameworks,[9] and $SnS_2/Sn_1\text{-}O_3G$[3] have been indicated to produce ethanol with a high selectivity in CO_2RR. However, the limited current density remains a critical challenge. Among the non-copper-based CO_2RR electrocatalysts, there has been a consensus on the high efficiency of Ag for *CO adsorption/desorption in CO_2RR.[10] Additionally, extensive research has been conducted on the adsorption of *CO on metal sites and early transition metal species such as Cr,[11,12] which demonstrate a strong adsorption ability for *CO intermediates. Therefore, the construction of asymmetric active sites containing Ag and Cr to promote *CO coupling is expected to enable ethanol production.[13] However, the competitive hydrogen evolution reaction (HER) is a much more serious concern for early transition metal species, as they produce H_2 as the dominant product. Thus, the suppression of the HER may be essential for the selective formation of ethanol on these asymmetric sites. On the other hand, recent advances in CO_2RR have highlighted the critical importance of controlling the interfacial microenvironment to enhance multi-carbon product selectivity while suppressing the competing HER on Cu-based materials.[14] However, current studies have mainly focused on regulating the interfacial water structure through metal cations,[15–17] whereas the role of the anions has received far less attention.[18] In fact, anions can also modulate the interfacial structure of water. For instance, Hofmeister series anions—ranked by their water-withdrawing effect for proteins—have been demonstrated to regulate the water structure,[19,20] thereby possibly affecting C–C coupling. More recently, ClO_4^- (which is identified as a water-structure breaker according to the Hofmeister series) has been demonstrated to promote the electrochemical reduction of CO to C_2H_4 on Cu-based catalysts.[21] However, the influence of anions on selective C–C coupling during CO_2RR over non-copper catalysts remains largely unexplored.

In this study, different anions were introduced to modulate the hydrogen-bond network on a copper-free Ag/Cr_2O_3 heterostructure with distinct active sites to achieve selective C–C coupling during CO_2RR. Ethanol was obtained on this non-copper-based catalyst, and the current densities for ethanol ($J_{ethanol}$) in electrolytes containing different anions followed the trend ClO_4^- (11.91 mA cm^{-2}) > NO_3^- (5.38 mA cm^{-2}) > NO_2^- (4.12 mA cm^{-2}) > $HCO_3^-/HPO_4^{2-}/SO_4^{2-}$ (hence no ethanol production) in a H cell, which is similar to the ability of Hofmeister series anions to disrupt hydrogen-bond networks.[22,23] Notably, the faradaic efficiency $(FE)_{ethanol}$ for an Ag/Cr_2O_3 catalyst reached ~50% at −0.7 V vs. a reversible hydrogen electrode (RHE) in a H cell, and it exhibited an $FE_{ethanol}$ of 51.8% at −0.8 V vs. RHE in a flow cell containing ClO_4^- with a stable response for 200 h at a current density of approximately 160 mA cm^{-2}, which is among the best performance for a non-Cu-based system in ethanol production. *In situ* spectroscopy and *ab initio* molecular dynamics (AIMD) simulations indicate that the introduction of ClO_4^- disrupts the continuous hydrogen-bonding network between water molecules, thereby inhibiting HER and enhancing the selectivity of CO_2RR toward ethanol production. Additionally, density functional theory (DFT) calculations demonstrate that the Ag–Cr asymmetric sites within the heterostructure are more favorable for *CO coupling and subsequent hydrogenation to form *OCCOH. Moreover, the free energy difference for the rate-determining step is reduced from 1.30 eV for the C_2H_4 pathway to 0.27 eV for the ethanol pathway, which results in the high selectivity toward ethanol production on Ag/Cr_2O_3.

RESULTS

Synthesis and structural characterization of electrocatalysts

The Ag/Cr_2O_3 heterostructured catalysts were synthesized via high-temperature calcination (450°C for 30 min) after the chemical precipitation of the nitrates of Ag and Cr. The catalysts with different Ag contents were labeled as Ag/Cr_2O_3, Ag/Cr_2O_3-2, and Ag/Cr_2O_3-3 (Table S1) according to X-ray fluorescence (XRF) analysis. Pure Ag and Cr_2O_3 samples were also prepared for comparison (Figure S1). The X-ray diffraction (XRD) patterns of the synthesized Ag/Cr_2O_3 and Ag/Cr_2O_3-2 samples (Figure S2) corresponded to the metallic Ag (PDF#01-1294, cubic phase) and Cr_2O_3 (PDF#01-1167, trigonal phase), which confirmed the successful synthesis of the heterostructures. However, Ag/Cr_2O_3-3 with a higher Ag content demonstrated characteristic peaks that corresponded to Ag_2CrO_4 (PDF#20-1055), which indicated a changed phase for this sample. Scanning electron microscopy (SEM) (Figures S3 and S4) showed that all samples were particles with sizes of around 100 nm except for pure Ag, which aggregated into large pieces. The energy dispersive X-ray spectroscopy (EDX) for Ag/Cr_2O_3 (Figure 1A) revealed a uniform distribution of Cr, O, and Ag elements, while high-resolution transmission electron microscopy (HR-TEM) images of Ag/Cr_2O_3 (Figure 1B) showed distinct lattice fringes with spacings of 0.236 and 0.367 nm that corresponded to Ag (111) and Cr_2O_3 (012), which further confirmed the formation of the heterostructure.

X-ray photoelectron spectroscopy (XPS) was performed to study the bond configuration of Ag/Cr_2O_3 (Figure S5). The Cr 2p spectra showed typical Cr(III) peaks at 586.1 and 576.5 eV,[24] which is similar to that of Cr_2O_3, while the O 1s peak was observed at 529.9 eV. However, the Ag 3d peaks in the Ag/Cr_2O_3 sample demonstrated a slightly lower binding energy

Please cite this article in press as: Liu et al., Interfacial hydrogen-bond network regulation enables selective CO_2 reduction to ethanol on copper-free electrocatalysts, Chem (2026), https://doi.org/10.1016/j.chempr.2026.103078

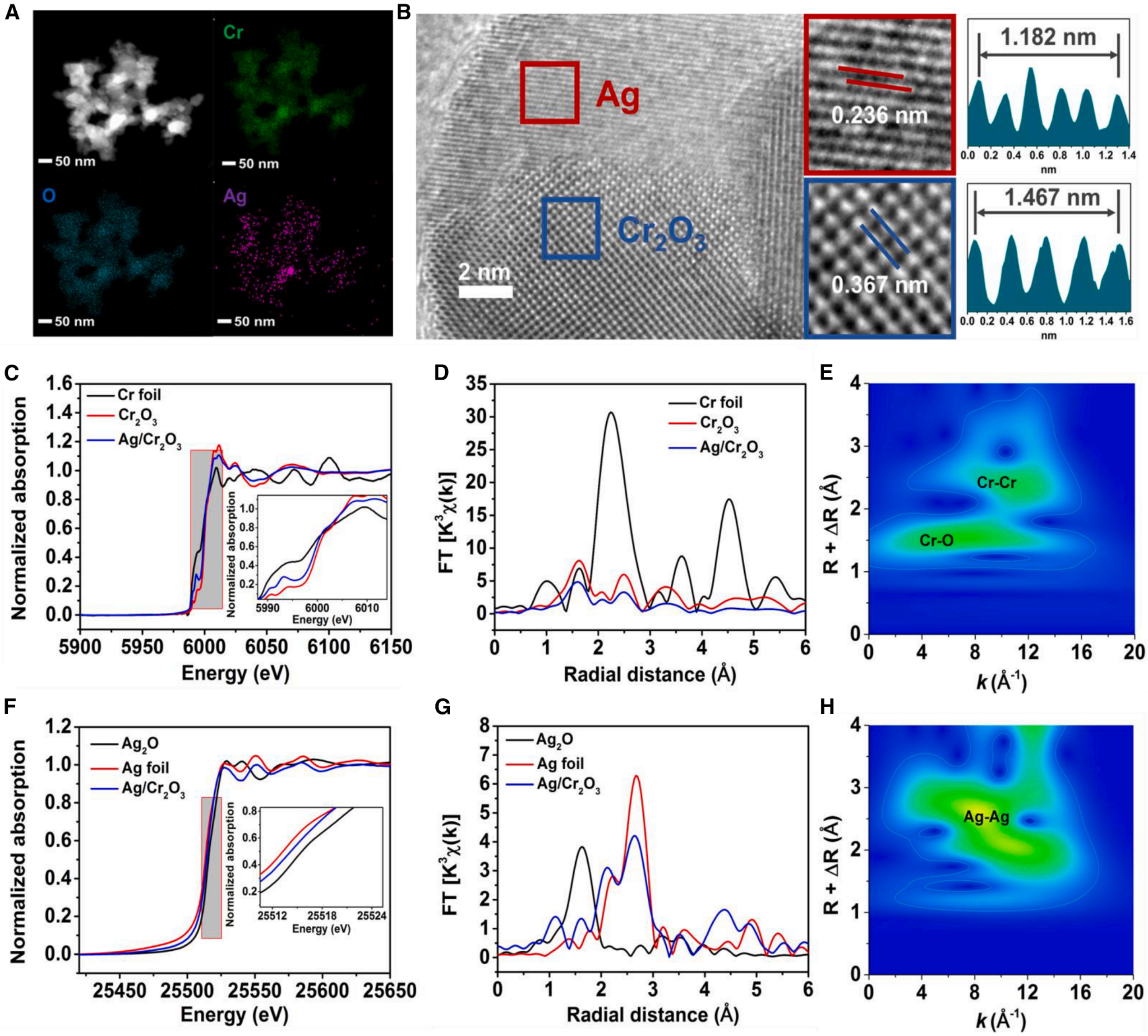

Figure 1. Structural and compositional characterization

(A) TEM image of Ag/Cr_2O_3 catalyst and the corresponding elemental mappings of Cr, Ag, and O.

(B) HR-TEM image of Ag/Cr_2O_3 catalyst.

(C) Cr K-edge XANES spectra of Ag/Cr_2O_3. (Insert) Magnification of the shadow region.

(D) Fourier transform of k^3-weighted Cr K-edge EXAFS spectra for the *r* space.

(E) Wavelet transform of the k^3-weighted EXAFS data of Cr K-edge for Ag/Cr_2O_3.

(F) Ag K-edge XANES spectra of Ag/Cr_2O_3. (Insert) Magnification of the shadow region.

(G) Fourier transform of k^3-weighted Ag K-edge EXAFS spectra for the *r* space.

(H) Wavelet transform of the k^3-weighted EXAFS data of Ag K-edge for Ag/Cr_2O_3.

(368.1 eV for Ag $3d_{5/2}$ peak) than that of metallic Ag (368.5 eV for Ag $3d_{5/2}$ peak), which indicated that Ag may undergo electron loss in the Ag/Cr_2O_3 heterostructure.[25] X-ray absorption spectroscopy (XAS) was employed to more precisely analyze the valence states and coordination environments of Cr and Ag in Ag/Cr_2O_3. As shown in Figure 1C, the X-ray absorption near edge structure (XANES) for the Cr K-edge in the Ag/Cr_2O_3 sample showed a quite small negative shift compared with that of pure Cr_2O_3, which suggests that the valence state of Cr in the Ag/Cr_2O_3 sample was slightly lower than that of Cr^{3+} in Cr_2O_3,[26] which is possibly due to the electron acquisition from Ag. The Fourier transform extended X-ray absorption fine structure (FT-EXAFS; Figure 1D) analysis and wavelet transform were performed on the Cr K-edge EXAFS results (Figures 1E, S6A, and S6B). The Ag/Cr_2O_3 sample showed scattering paths that were associated with Cr–O and Cr–Cr, which is similar to Cr_2O_3. On

Please cite this article in press as: Liu et al., Interfacial hydrogen-bond network regulation enables selective CO_2 reduction to ethanol on copper-free electrocatalysts, Chem (2026), https://doi.org/10.1016/j.chempr.2026.103078

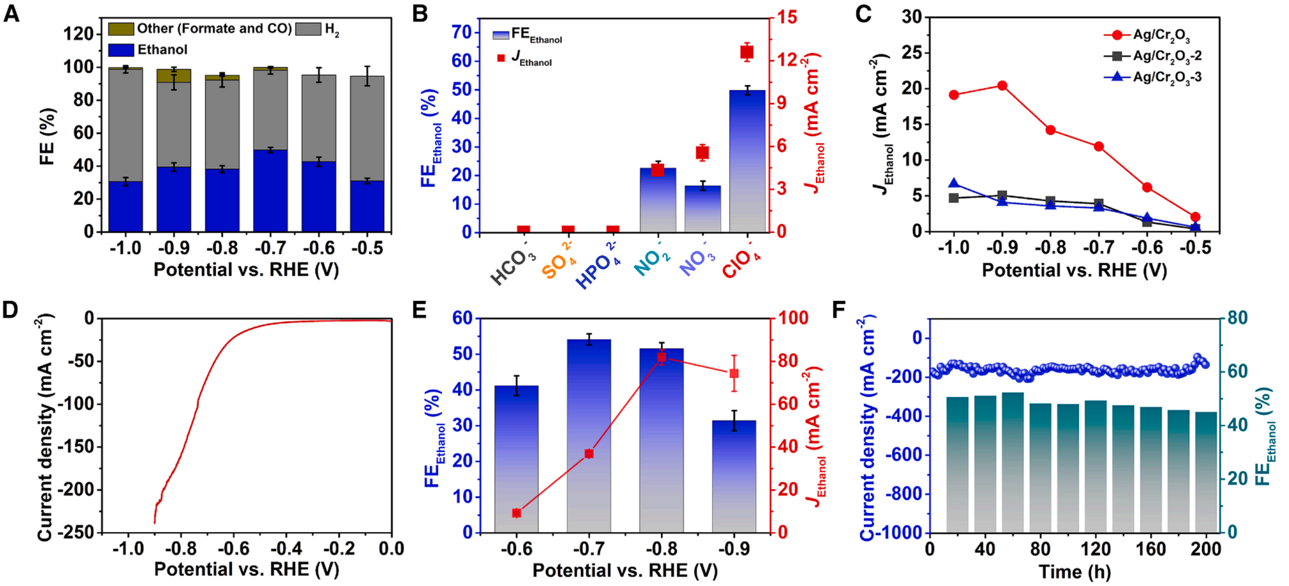

Figure 2. CO_2RR performance of the Ag/Cr_2O_3 catalyst

(A) FE of different products for Ag/Cr_2O_3 in a H cell. The error bars represent the standard deviation for three independent measurements.

(B) $FE_{ethanol}$ for Ag/Cr_2O_3 in 0.5 M $KHCO_3$ with different anions added in a H cell at −0.7 V vs. RHE. The error bars represent the standard deviation for three independent measurements.

(C) $J_{ethanol}$ for Ag/Cr_2O_3-X in a H cell. Ethanol cannot be detected for the Ag and Cr_2O_3 control samples.

(D) Linear sweep voltammetry (LSV) curves for the Ag/Cr_2O_3 catalyst in the flow cell.

(E) $FE_{ethanol}$ at different potentials in the flow cell. The error bars represent the standard deviation for three independent measurements.

(F) Stability test during 200 h of electrolysis at −0.8 V vs. RHE in the flow cell.

the other hand, the XANES spectrum for Ag K-edge in the Ag/Cr_2O_3 sample lay between that of pure Ag and Ag_2O (Figure 1F), thus indicating that the valence state of Ag was slightly higher than that of metal Ag, which was consistent with the XPS analysis. Additionally, FT-EXAFS (Figure 1G) and wavelet transform (Figures 1H, S6C, and S6D) indicated that the Ag component in Ag/Cr_2O_3 was similar to pure Ag, which exhibited a Ag–Ag scattering path but lacked the Ag–O scattering path found in Ag_2O. These results collectively demonstrate that the Ag/Cr_2O_3 catalyst possesses a heterostructure with an electronic interaction between Ag and Cr species, which potentially enhances the electrocatalytic performance of CO_2RR.[27]

Catalytic performance of Ag/Cr_2O_3 for CO_2RR

The CO_2 electrocatalytic activity of Ag/Cr_2O_3 was evaluated in a H-type cell. As shown in Figure S7A, the addition of ClO_4^- increased the current density of the Ag/Cr_2O_3 catalyst, which indicated that it may promote CO_2RR. ^1H NMR spectra tests revealed that ethanol was generated on the Ag/Cr_2O_3 catalyst across a wide potential range of −0.5 to −1.0 V vs. RHE (Figures 2A and S7B), with the highest FE for ethanol of ~50% at −0.7 V vs. RHE and a partial current density ($J_{ethanol}$) of 11.9 mA cm^{-2} in the CO_2-saturated 0.5 M potassium bicarbonate ($KHCO_3$) electrolyte containing ClO_4^-. The main byproduct was gas-phase H_2 for Ag/Cr_2O_3, while the other byproducts were negligible (1.9% for formate and 0.4% for CO at −0.7 V vs. RHE). The electrochemical performance of Ag/Cr_2O_3 in the argon atmosphere was also evaluated (Figures S7C and S7D), and the result showed that the only product was H_2, which indicated that $KHCO_3$ itself does not participate in the C–C coupling. In addition, Ag/Cr_2O_3 was also tested in a CO_2-saturated $KClO_4$ electrolyte without $KHCO_3$ (Figures S8A–S8C), and the results demonstrated that ethanol could be obtained in a 0.05 M $KClO_4$ electrolyte without liquid byproducts, which indicated that the presence of ClO_4^- effectively promoted C–C coupling. However, the achieved current densities were quite low, which was possibly due to the high resistance of the electrolyte. Furthermore, the effects of various anions (SO_4^{2-}, HPO_4^{2-}, NO_2^-, and NO_3^-) in 0.5 M $KHCO_3$ for CO_2RR were also investigated. As shown in Figures 2B and S8D–S8I and Table S2, no ethanol was produced when SO_4^{2-} and HPO_4^{2-} were present in a 0.5 M $KHCO_3$ solution, while ethanol could be generated in the presence of NO_2^- and NO_3^-. However, their $FE_{ethanol}$ and $J_{ethanol}$ were lower than that of ClO_4^-, and side reactions (the reduction of NO_2^- and NO_3^-) existed (Figures S8E and S8F). Moreover, the $J_{ethanol}$ for different anions followed the order: ClO_4^- (11.91 mA cm^{-2}) > NO_3^- (5.38 mA cm^{-2}) > NO_2^- (4.12 mA cm^{-2}) > $HCO_3^-/HPO_4^{2-}/SO_4^{2-}$, which aligned with the trend observed in the Hofmeister series,[28,29] where anions with stronger water-structure-destabilizing effects tend to enhance ethanol production. The CO_2RR performance of Ag/Cr_2O_3 was also evaluated in a 0.5 M $KHCO_3$ electrolyte with the addition of halide ions (Cl^-, Br^-, and I^-), which was due to the halide-induced structural reconstruction of Ag, although negligible ethanol (<2%) could be detected (Figures S9 and S10). Additionally, the performance of Ag/Cr_2O_3 with different Ag contents in

Please cite this article in press as: Liu et al., Interfacial hydrogen-bond network regulation enables selective CO_2 reduction to ethanol on copper-free electrocatalysts, Chem (2026), https://doi.org/10.1016/j.chempr.2026.103078

ethanol production was evaluated. As shown in Figures 2C and S11, the $FE_{ethanol}$ and $J_{ethanol}$ of Ag/Cr_2O_3 were significantly higher than those of Ag/Cr_2O_3-2 (23.3%, 3.9 mA cm^{-2}), Ag/Cr_2O_3-3 (16.8%, 3.3 mA cm^{-2}), Cr_2O_3 (no ethanol generation), and Ag (no ethanol generation). Furthermore, the electrochemical surface area (ECSA) of different catalysts was evaluated to assess the relationship between ethanol production of the catalyst and its specific surface area. As shown in Figure S12, these catalysts generally showed similar ECSA values, which indicated that it was the intrinsic catalytic sites rather than the ECSA that promoted the formation of ethanol. Ag and Cr_2O_3 were also physically mixed to test its ethanol production performance (Figures S13 and S14). Its current density was significantly reduced, and almost no ethanol was generated, which suggested that the abundant heterostructure interface of Ag/Cr_2O_3 was essential for effective ethanol production.

A flow cell was further assembled to achieve a high current density for the production of ethanol with Ag/Cr_2O_3 as the catalyst in the presence of ClO_4^-. As shown in Figures 2D and 2E, the current density significantly increased to hundreds of mA cm^{-2} in the flow cell with the highest $J_{ethanol}$ of 82.4 mA cm^{-2} and a $FE_{ethanol}$ of 51.8% at -0.8 V vs. RHE, which outperformed most of the non-Cu systems for ethanol production (Table S3). Additionally, almost no formate peak was detected in the ^1H NMR spectra for the flow cell (Figure S15), which further certified the high selectivity of this system for ethanol formation. Moreover, Ag/Cr_2O_3 maintained a stable current density of approximately 160 mA cm^{-2} for over 200 h with no significant $FE_{ethanol}$ decay (Figure 2F), thus demonstrating its excellent stability.

Mechanism study

Raman spectroscopy was used to investigate the changes in water structure on an Ag/Cr_2O_3 catalyst at -0.7 V vs. RHE in CO_2-saturated electrolytes. Pure $KHCO_3$ solution and $KHCO_3$ solutions containing representative anions (ClO_4^- and HPO_4^{2-}) were selected to conduct the mechanism investigation. The O–H stretching vibrations in the range of 3,000–3,800 cm^{-1} were divided into three characteristic peaks (Figures 3A and S16), which corresponded to the three types of water molecules[30]: ~3,230 cm^{-1} for water with strong hydrogen bonding (4-HB·H_2O), ~3,450 cm^{-1} for water with weak hydrogen bonding (2-HB·H_2O), and ~3,640 cm^{-1} for cation-bound water (K·H_2O). Based on the integrated areas, the addition of 0.05 M dipotassium hydrogen phosphate (K_2HPO_4) to 0.5 M $KHCO_3$ did not lead to significant changes in the proportions of these water structures. However, the proportions of 4-HB·H_2O and cation-bound water decreased from 32.2% and 7.6% to 24.8% and 3.8%, while the proportion of 2-HB·H_2O increased from 60.2% to 71.4% when 0.05 M $KClO_4$ was added to 0.5 M $KHCO_3$. This indicated that the formation of hydrogen bonds between ClO_4^- and H_2O disrupted the original hydrogen-bond network between water molecules.[31] Furthermore, the impact of these anions on HER activity was explored by conducting LSV tests of Ag/Cr_2O_3 catalyst in argon-saturated 0.5 M $KHCO_3$ solutions containing either HPO_4^{2-} or ClO_4^-. As shown in Figure S17, the addition of HPO_4^{2-} resulted in almost no change in LSV curve, which indicated that this anion did not suppress HER. However, the current density decreased when ClO_4^- was added, thus suggesting that HER was inhibited, which was consistent with the analysis of the water structure. AIMD simulations were employed to further investigate the role of different anions in the hydrogen-bond network. Figures 3B, S18, and S19 showed the structural snapshots of Cr_2O_3 (the main component of the catalyst) in the electrolytes containing $KHCO_3$ + $KClO_4$, $KHCO_3$, and $KHCO_3$ + K_2HPO_4, respectively. It could be found that H and O atoms were located farthest from the catalyst surface when ClO_4^- was present in the electrolyte (Figures 3C and 3D), which matched the reduced proportion of cation-bound free water for ClO_4^- in Raman spectroscopy and may be unfavorable for HER.[32] In contrast, HPO_4^{2-} and HCO_3^- exhibited similar distributions, with atoms located closer to the surface. The number of hydrogen bonds in the three electrolytes was also analyzed (Figure 3E). It is generally accepted that a continuous hydrogen-bond network between water molecules facilitates proton migration, thus enhancing hydrogen evolution at the electrode/electrolyte interface.[33] When ClO_4^- was introduced, the number of hydrogen bonds closest to the surface decreased, which indicated that ClO_4^- disrupted the original hydrogen-bond network as well as inhibited the adsorption of hydrogen. This disruption would hinder HER and provide a favorable environment for CO_2 activation and C–C coupling. It was also noticed that the ethanol current density increased significantly with the presence of ClO_4^- (Figure 2B). A possible reason is that HER and CO_2RR may share similar active sites for Ag/Cr_2O_3. The inhibited HER would leave room for more C-bound surface species on the catalyst, thus resulting in promoted C–C coupling.

In situ attenuated total reflection Fourier transform infrared spectroscopy (ATR-FTIR) was performed on an Ag/Cr_2O_3 catalyst to investigate the reaction intermediates in electrolytes containing different anions (Figures 3F–3H). In a 0.5 M $KHCO_3$ + 0.05 M $KClO_4$ electrolyte, a series of characteristic absorption bands associated with CO_2 reduction emerged in the 1,200–2,000 cm^{-1} region as the potential was applied. The two bands at around 1,410–1,560 cm^{-1} are likely attributed to the symmetric and antisymmetric stretching vibration of COO structures such as carboxylate groups.[34,35] Even though the bands can be related to the conversion of formate,[36] we suggest that formate species would not be the dominant candidate since the FE of formate is quite low during CO_2RR. In addition, activated CO_2 with a COO structure may also be the possible candidate,[36,37] as the adsorption/activation of CO_2 always exists in CO_2RR. The band at around 1,700 cm^{-1} (which is also verified by the time-dependent measurement at -0.7 V vs. RHE; Figure S20) is assigned to the stretching vibration of species with a C=O bond,[34,35] such as CO_2 adsorbed species and intermediates with a carboxyl group or an aldehyde group. The two peaks at around 1,700 cm^{-1} may be attributed to the C=O species with different chemical environments (for example, the unsaturated groups or hydrogen bonds that would lead to a red shift for the band of C=O).[34] However, these bands were not discernible in the CO_2-saturated 0.5 M $KHCO_3$ electrolyte and 0.5 M $KHCO_3$ containing HPO_4^{2-}. C_{2+} products were also not detected for the Ag/Cr_2O_3 catalyst in these electrolytes (Figures S8G and S8I). Therefore, we can conjecture that CO_2 is activated and reduced on Ag/Cr_2O_3 in the electrolyte containing perchlorate, with the formation of C=O-containing

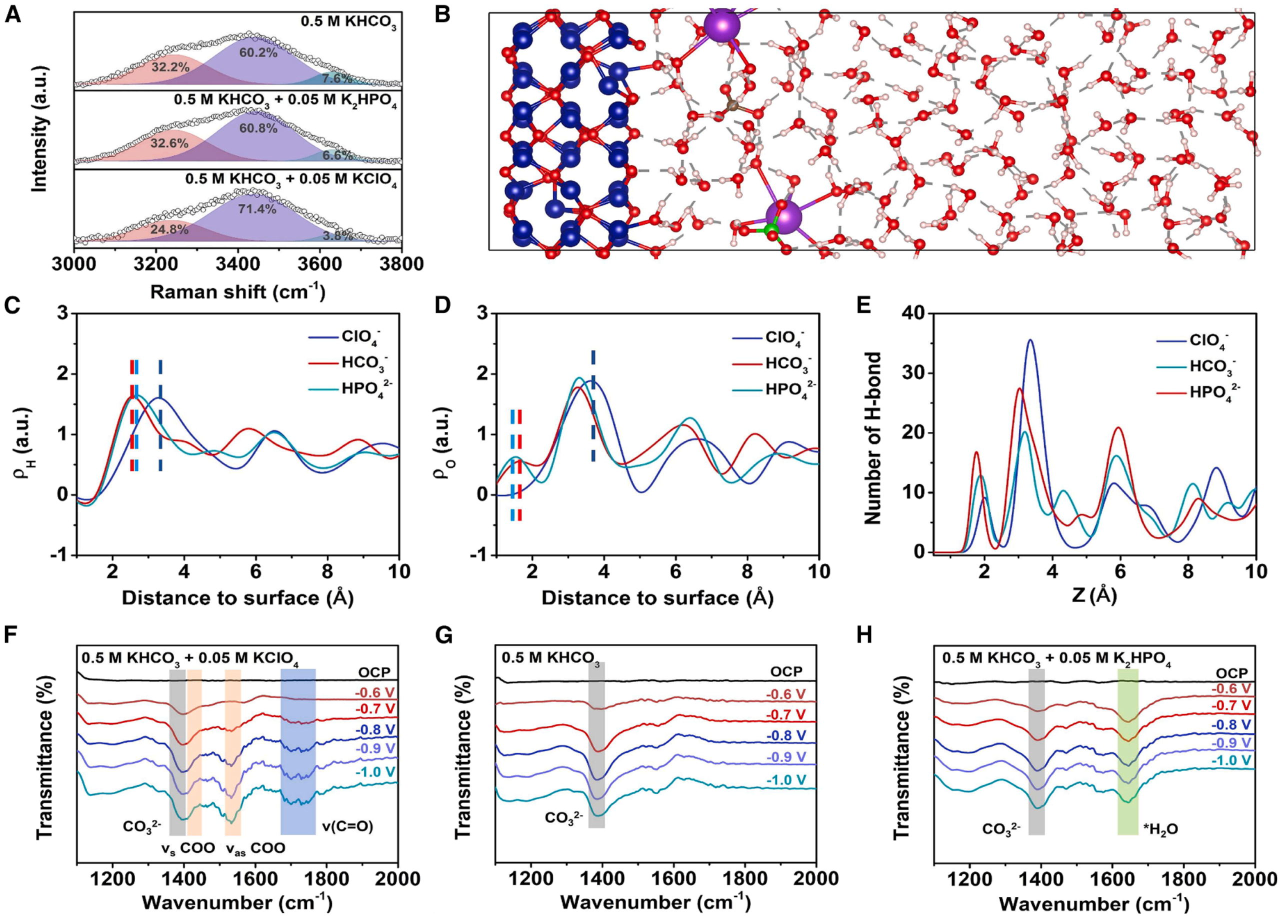

Figure 3. Exploration of interface water structure

(A) Raman spectra for Ag/Cr_2O_3 at −0.7 V vs. RHE in a CO_2-saturated different electrolyte.

(B) Snapshot of water structure in the $KHCO_3$ + $KClO_4$ solution, with atom colors being Cr in blue, C in brown, H in pink, O in red, Cl in green, and K in purple.

(C) Distribution of H atoms in electrolytes containing different anions.

(D) Distribution of O atoms in electrolytes containing different anions.

(E) Number of hydrogen bonds in electrolytes containing different anions.

(F–H) *In situ* ATR-FTIR for Ag/Cr_2O_3 in 0.5 M $KHCO_3$ + 0.05 M $KClO_4$ (F), 0.5 M $KHCO_3$ + 0.05 M K_2HPO_4 (G), and 0.5 M $KHCO_3$ (H).

intermediates that further contribute to the formation of ethanol. Nevertheless, it should be admitted that the assignment of these bands to specific C–C coupling intermediates is quite difficult.

In addition to anions, the component of the catalyst also affects its catalytic performance for ethanol electrosynthesis. *In situ* Raman and infrared spectroscopy were conducted on catalysts with different components to further investigate the possible mechanism of CO_2RR. As shown in Figures S21 and S22, weak bands that corresponded to COO- and C=O-containing species[34] were recorded for Ag/Cr_2O_3. In addition, a broad band at 2,800–3,000 cm^{-1} that was assigned to the stretching vibrations of CH_x species[34,38,39] was also observed on both Raman and infrared spectra for Ag/Cr_2O_3 (Figures S23 and S24), which suggested the possible formation of hydrogenated carbon species during the reaction. However, no peak corresponding to C=O or CH_x species was observed for either Cr_2O_3 or Ag (ethanol was also not detected in the two samples; Figure S11). Their results indicate that it is the Ag-Cr asymmetric sites rather than simple Ag or Cr that contribute to the formation of ethanol. Since pure Ag promotes CO formation but does not undergo C–C coupling (Figure S11C), it is likely that CO_2RR intermediates may be active on the Ag sites and further spill over to the Cr_2O_3 sites, thus facilitating C–C coupling. The potential benefit of the Cr_2O_3 component (HER as the dominant reaction without Ag; Figure S11D) in Ag/Cr_2O_3 for ethanol formation was also analyzed. Previous studies have shown that Cr_2O_3 readily adsorbs OH species,[40] and the promoted *OH coverage may stabilize the CO_2RR intermediates and contribute to selective ethanol formation.[41] The OH adsorption peaks of the Cr_2O_3 component in this work were also verified in the LSV curves[42] (Figure S25) and the Raman signal at 730 cm^{-1}[40,43] (Figure S26). Meanwhile, Ag/Cr_2O_3 and Cr_2O_3 displayed higher local pHs (Figures S27 and S28) compared with the Ag sample,[44] which further certified their stronger affinity for OH. Based on these results, it can be inferred that the Ag component activates CO_2 to form a *CO intermediate, part of which spills over to the Cr_2O_3 component, while Cr_2O_3 with

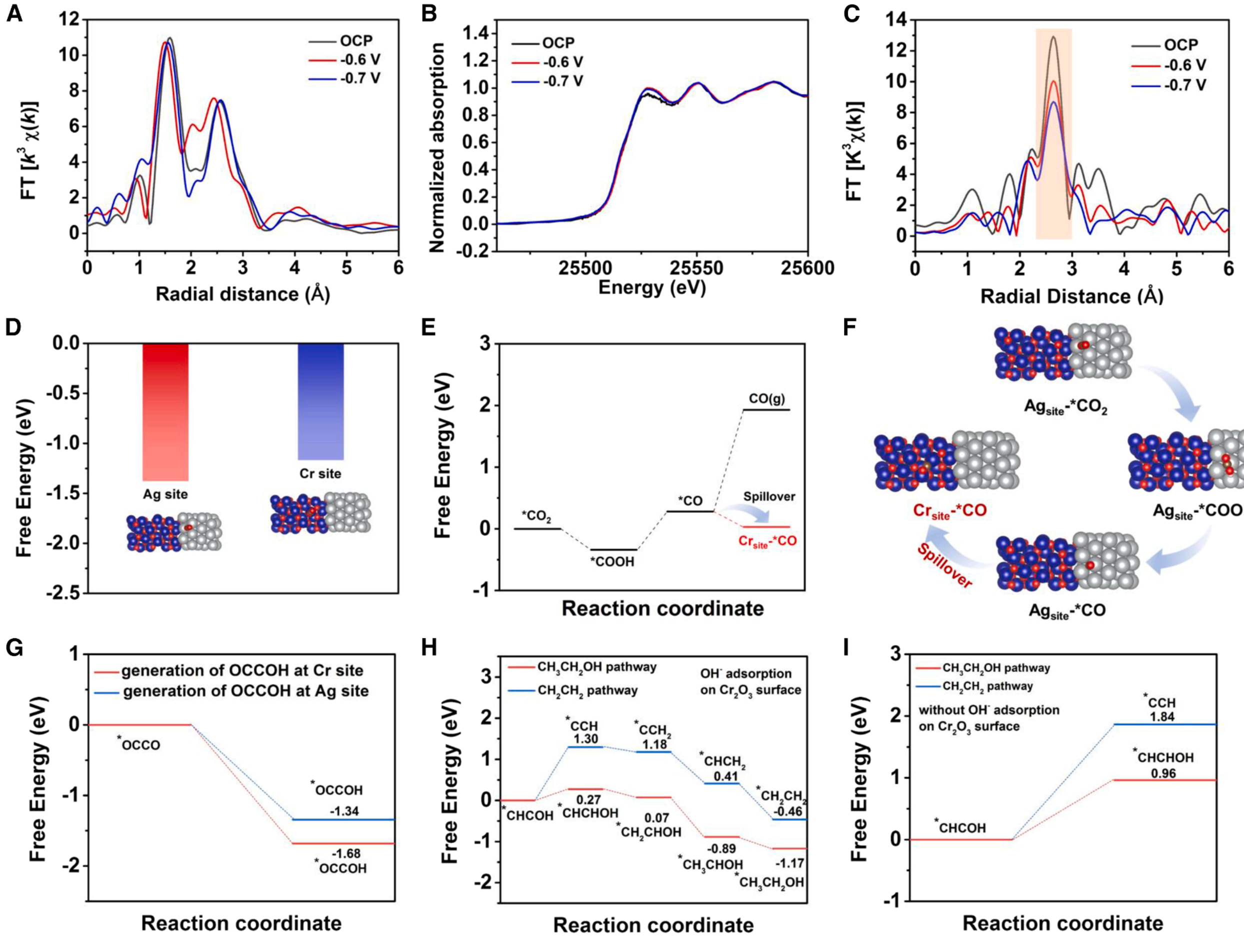

Figure 4. Mechanism investigation

(A) Fourier transform of k^3-weighted Cr K-edge EXAFS spectra for the *r* space at various potentials.

(B) *In situ* Ag K-edge XANES spectra.

(C) Fourier transform of k^3-weighted Ag K-edge EXAFS spectra for the *r* space at various potentials.

(D) CO_2 adsorption on different sites for Ag/Cr_2O_3.

(E) DFT calculations for CO spillover path.

(F) Schematic diagram of CO spillover path (Ag atom, silver; Cr atom, blue; O atom, red; H atom, pink; C atom, brown).

(G) DFT calculations for the formation of *OCCOH at different sites on Ag/Cr_2O_3 with surface adsorption of *OH.

(H) Ethanol and ethylene pathways on Ag/Cr_2O_3 with the surface adsorption of *OH.

(I) The conversion of *CHCOH via ethanol or ethylene pathways on Ag/Cr_2O_3 without the surface adsorbed *OH.

partial adsorbed *OH would stabilize the CO_2RR intermediates and facilitate the asymmetric hydrogenation during C–C coupling to produce ethanol on Ag/Cr_2O_3.

In situ XAS was employed to reveal the potential structural and local coordination environment changes of the Ag/Cr_2O_3 catalyst during CO_2RR (Figures 4A–4C and S29–S35). As shown in Figure S29, there is no significant shift in the relative absorption edge position of the Cr K-edge XANES after applying the potential, and the FT-EXAFS spectra (Figure 4A) display Cr–O and Cr–Cr bonds that are characteristic of Cr_2O_3. Moreover, Table S4 shows that the coordination number and bond length of Cr–O exhibit almost no change before and after the application of the potential, thus indicating the structural stability of Cr_2O_3. The shift of the relative absorption edge position in the Ag K-edge XANES is also negligible (Figure 4B). However, the coordination number of Ag–Ag decreases from 11.8 at open-circuit potential (OCP) to 9.8 at an applied potential of −0.7 V (Figure 4C; Table S5), which suggests the presence of unsaturated Ag species at this potential. These vacancies may facilitate CO_2 adsorption and activation, thereby providing more *CO intermediates for further reactions.[45] Additionally, the XRD (Figure S36) shows that the Ag/Cr_2O_3 catalyst retains its cubic Ag and trigonal Cr_2O_3 phases after CO_2RR, which indicates that the catalyst generally maintains its structural stability during CO_2RR.

To gain a deeper insight into the nature of the active sites and the interfacial synergistic mechanism, DFT calculations were conducted on the Ag/Cr_2O_3 heterostructure (Figures 4D–4I and

Please cite this article in press as: Liu et al., Interfacial hydrogen-bond network regulation enables selective CO_2 reduction to ethanol on copper-free electrocatalysts, Chem (2026), https://doi.org/10.1016/j.chempr.2026.103078

S37–S39), and the preferential adsorption sites of CO_2 on Ag/Cr_2O_3 were explored. As shown in Figures 4D–4F, CO_2 would primarily adsorb on the Ag sites (−1.38 eV) instead of the Cr sites (−1.17 eV) for the Ag/Cr_2O_3 catalyst. Subsequently, the adsorbed $^*CO_2$ undergoes a proton-coupled electron transfer process at the Ag site to form *CO. Notably, the thus-formed *CO preferentially migrates to the Cr site (−0.25 eV) rather than desorbing as CO (1.65 eV), thus indicating the energetic preference of the *CO intermediate spillover from Ag to Cr, which matches the hypothesis in spectra data analysis. Additionally, the hydrogenation behavior of the *OCCO intermediate (which is generally suggested to be the key intermediate for C–C coupling[19,46–48]) at asymmetric interfacial sites was examined to further reveal the pathway for ethanol formation. As illustrated in Figures 4G and S37, the free energy difference is −1.68 eV when the *CO adsorbed at the Cr site is hydrogenated for the *OCCO intermediate, which is much lower than the free energy difference of −1.34 eV for the hydrogenation of *OCCO at the Ag site, thus indicating that the *OCCO intermediate is preferentially first hydrogenated at the Cr site to form *OCCOH, which then undergoes further proton-coupled electron transfer. Moreover, ethylene is a common competitive product in the ethanol formation process since the two products share the same *CHCOH intermediate, and DFT calculations were performed to explore the two possible pathways (from *CHCOH to ethanol and ethylene; Figures 4H and S38) to reveal the reason for the high selectivity toward ethanol on the Ag/Cr_2O_3 heterostructure. The results show that when *CHCOH is further hydrogenated to *CHCHOH (the ethanol pathway), the free energy difference is only 0.27 eV, while the free energy difference for the ethylene pathway (*CCH) is as high as 1.30 eV, which indicates the reduced energy barrier for the ethanol pathway. To verify the promoting effect of *OH on ethanol formation, DFT calculations were also applied for the Ag/Cr_2O_3 heterostructure without *OH adsorption. As shown in Figures 4I and S39, the Ag/Cr_2O_3 heterostructure still favors ethanol formation over ethylene even without *OH adsorption. However, the free energy for *CHCHOH formation on the Ag/Cr_2O_3 heterostructure increases to 0.96 eV without the presence of an adsorbed neighbor *OH, which verifies that the partially adsorbed *OH on Cr_2O_3 effectively reduces the free energy required for the formation of the key intermediate *CHCHOH in the ethanol pathway, thus further enhancing the selectivity for ethanol.

In order to validate the universality of ethanol production by modulating the catalyst/electrolyte interface with ClO_4^- for non-copper-based heterostructured electrocatalysts in CO_2RR, Ag/ZnO, Ag/VO_x, Ag/MnO_2, and Ag/WO_3 (Figure S40) were prepared and tested, as these catalysts have been reported either to facilitate the formation of *CO intermediates or to exhibit strong binding affinities toward CO species. The results revealed that all these catalysts are capable of producing ethanol, with an $FE_{ethanol}$ consistently exceeding 30% when ClO_4^- is present in the electrolyte. Furthermore, the Cr_2O_3 component is replaced by p-block metal oxides that predominantly generate *OCHO intermediates during CO_2RR, such as Bi_2O_3, In_2O_3, and SnO_2. The liquid products are mainly formate. No ethanol is detected on the Ag/Bi_2O_3 catalyst, and the FEs for ethanol on Ag/In_2O_3 and Ag/SnO_2 are also very low (<10%). In addition to ethanol and formate, hydrogen can be detected in all the samples due to the competitive HER. These results indicate that the introduction of ClO_4^- to modulate the catalyst/electrolyte interface may be a universal strategy for achieving C–C coupling on non-copper-based materials for CO_2RR, and creating asymmetric tandem active sites that prefer *CO intermediate adsorption/conversion may be the key factor for achieving selective ethanol formation.

DISCUSSION

In summary, we propose a strategy that is based on anion regulation at the electrode/electrolyte interface to induce selective ethanol electrosynthesis on non-Cu catalysts during CO_2RR. *In situ* spectroscopy and AIMD simulations reveal that ClO_4^- disrupts the interfacial hydrogen-bonding network by reducing the number of hydrogen bonds, thereby suppressing HER and potentially promoting C–C coupling on non-copper-based Ag/Cr_2O_3 electrocatalysts. DFT calculations and *in situ* characterizations suggest that the Ag–Cr asymmetric active sites favor the activation and conversion of C=O-containing species during CO_2RR, and thus substantially reduce the free energy difference for the rate-determining step of ethanol formation to 0.27 eV (1.30 eV for the ethylene pathway), which endows the Ag/Cr_2O_3 catalyst with a high selectivity toward ethanol. In electrolytes that contain different anions, the $J_{ethanol}$ of the Ag/Cr_2O_3 catalyst follows the trend of ClO_4^- (11.91 mA cm^{-2}) > NO_3^- (5.38 mA cm^{-2}) > NO_2^- (4.12 mA cm^{-2}) > HCO_3^-/HPO_4^{2-}/SO_4^{2-} (no ethanol production) in a H cell, which is similar to the ability of Hofmeister series anions to disrupt hydrogen-bond networks. In a flow cell containing ClO_4^-, the Ag/Cr_2O_3 catalyst exhibited an $FE_{ethanol}$ of 51.8% and a $J_{ethanol}$ of 82.4 mA cm^{-2} at −0.8 V vs. RHE, and it can be stably operated for 200 h at a current density of about 160 mA cm^{-2}, which is one of the best results for non-Cu-based materials. We believe that this work would extend the non-Cu electrocatalysis system for CO_2RR to achieve C–C coupling, and it would provide valuable insights for the future design of efficient non-Cu-based catalysts as well as the regulation of catalyst/electrolyte interfaces with anions for CO_2RR.

METHODS

Materials

Chromium nitrate ($Cr(NO_3)_3{\cdot}9H_2O$, Innochem, 99.9%); silver nitrate ($AgNO_3$, Chengdu Kelong, ≥ 99.8%); sodium borohydride ($NaBH_4$, Aladdin, ≥98%); potassium hydroxide (KOH, Aladdin, 99.5%); perchloric acid ($HClO_4$, Sinopharm Chemical Reagent, analytical reagent); potassium nitrate (KNO_3, Aladdin, 99.0%); potassium nitrite (KNO_2, Innochem, 97%); $KHCO_3$ (Aladdin, 99.5%), K_2HPO_4 (Aladdin, 99.0%); and potassium sulfate (K_2SO_4, Aladdin, 99.0%). Ethanol (analytical reagent) was used without any further purification, and the ultra-pure water (18.25 MΩ cm^{-1}) used in all experiments was prepared by an ultrapure purification system (Ulupure).

Synthesis of Ag/Cr_2O_3, Ag, and Cr_2O_3

For Ag/Cr_2O_3-X, 0.246 g of $Cr(NO_3)_3{\cdot}9H_2O$ and different quantities of $AgNO_3$ were added to 50 mL of water in a glass beaker,

Please cite this article in press as: Liu et al., Interfacial hydrogen-bond network regulation enables selective CO_2 reduction to ethanol on copper-free electrocatalysts, Chem (2026), https://doi.org/10.1016/j.chempr.2026.103078

and the mixture was stirred continuously to form solution A. 0.064 g of $NaBH_4$ was dissolved in water to form solution B. Solution A was stirred vigorously while solution B was slowly added dropwise. After 30 min of reaction, the mixture was centrifuged and washed with ethanol and deionized water, and it was then placed in an oven at 80°C for 12 h to dry. Finally, high-temperature calcination was performed in a tubular furnace at 450°C for 30 min. And during the synthesis process of pure Ag and Cr_2O_3, $Cr(NO_3)_3 \cdot 9H_2O$, and $AgNO_3$ were not added, respectively, and other conditions were the same as for Ag/Cr_2O_3-X.

Preparation of WEs

The electrocatalysts (1 mg) and Vulcan XC-72 carbon powder (4 mg) were dispersed in a mixture of 500 μL isopropyl alcohol and 20 μL of 5% Nafion solution. Ultrasonic treatment of the above mixture was performed for 60 min to obtain a uniform suspended ink. The ink was evenly dripped onto both sides of a piece of carbon paper (about 1.0 × 1.0 cm) and then vacuum dried at 60°C for 1 h to obtain a working electrode (WE). The effective catalyst loading is approximately 0.2 mg.

Characterizations

The morphologies and compositional elements were confirmed by SEM using the model Sirion 200. TEM was carried out on a Tecnai G2 TEM (Thermo Scientific, USA). HR-TEM characterizations were obtained via a Talos F200X TEM (Thermo Scientific, USA). XRD patterns were obtained via a DMAX-2400 X-ray diffractometer (Rigaku, Japan). Raman measurements were performed using Renishaw inVia Raman microscope system with 532-nm excitation wavelength. XPS was carried out with an Axis-Ultra DLD-600W X-ray photoelectron spectrometer (Shimadzu, Japan). The ^1H NMR spectra were performed on a Bruker Ascend 600 MHz. D_2O was utilized as the deuterium reagent; 500 μL of the electrolyte was mixed with 100 μL DMSO (0.05 μL/mL) and then dissolved in 150 μL D_2O solution, and DMSO was used as the internal standard solution. *In situ* ATR-FTIR was performed using a Nicolet iS50R spectrometer (Thermo Scientific, USA). XAS was determined by the Shanghai Synchrotron Radiation Facility (SSRF) at the beamline BL11B1. XRF patterns were obtained from EAGLE III operated at 40 kV. A UV spectrophotometer with the model TU-1810 was used to obtain absorbance.

Electrochemical tests

H-type cell

Electrochemical tests were first performed in a three-electrode, two-compartment H cell controlled by an electrochemical workstation (CHI 660e, Chenhua). Two chambers were separated by a proton exchange membrane (Nafion 212, Dupont). The WE was catalyst-loaded carbon paper. An Ag/AgCl electrode (saturated KCl solution) and a graphite rod were used as the reference electrode (RE) and counter electrode (CE). The CO_2-saturated 0.5 M $KHCO_3$ + 0.05 M $KClO_4$ solution (40 mL) was applied as the electrolyte, and the flow rate of CO_2 during the test was maintained at 20 mL/min. During the test, the cathode chamber electrolyte was stirred at 600 rpm. All the electrode potentials were measured against the Ag/AgCl electrode and converted to the RHE by $E_{RHE} = E_{Ag/AgCl} + 0.197 + 0.059 \times pH$, where pH is the average pH value of the electrolyte. ECSA was estimated according to ECSA = C_{dl}/C_s, where the double-layer capacitance (C_{dl}) of the catalysts was obtained from cyclic voltammetry measurements conducted in the non-faradaic region by analyzing the capacitive current densities at varying scan rates in CO_2-saturated 0.5 M $KHCO_3$ + 0.05 M $KClO_4$ solution, and the value corresponds to half of the slope derived from the linear fit of current density vs. scan rate, and C_s is the specific capacitance of a flat carbon surface with 1 cm^2 of real surface area. All electrochemical measurements in the H cell did not have any current-resistance (iR) compensation. Further details regarding the product analysis can be found in the supplemental methods.

Flow cell

A gas-diffusion flow cell consisting of a gas-diffusion layer (TGP-H-060, 20% polytetrafluoroethylene, TORAY) deposited with Ag/Cr_2O_3-X (1.0 cm^2) as the WE, nickel foam (1 mm, 1.0 cm^2) as the CE, and Ag/AgCl (saturated KCl solution) as the RE was constructed. A 1.0 M KOH + 0.05 M $KClO_4$ solution (100 mL) was used as the electrolyte. The electrolyte was maintained at 64 mL/min during electrolysis. Preparation of gas-diffusion electrode was as follows: the electrocatalysts (1 mg) and Vulcan XC-72 carbon powder (4 mg) were dispersed in a mixture of 500 μL isopropyl alcohol and 20 μL of 5% Nafion solution. Ultrasonic treatment of the above mixture for 60 min was used to obtain a uniform suspended ink. The ink was evenly dripped on one side of the gas-diffusion layer (1.0 cm^2) to obtain a gas-diffusion electrode. The effective catalyst loading is approximately 0.5 mg. Cathode and anode channels were separated by a proton exchange membrane (Nafion 212, Dupont). In the gas channel, the flow rate of CO_2 during test was maintained at 20 mL/min.

In situ measurements

In situ Raman spectroscopy was performed on a Renishaw inVia Raman microscope system with *in situ* Raman gas-diffusion H-type electrolytic cell (Gaossunoin, China). The wavelength of the excitation source of the laser is 532 nm (50%). A 50× long focal length distance objective (Leica) was used for focusing. The WE was prepared according to the "preparation of WEs" section, with a catalyst layer thickness of approximately 5.9 μm (Figure S41). An Ag/AgCl electrode (saturated KCl) and a graphite rod served as the RE and CE, respectively. The spectrum was collected after 10 min of stable operation for each potential. The corresponding current responses recorded during the *in situ* Raman measurements in different electrolytes have been added in Figure S42.

In situ *ATR-FTIR*

In situ electrochemical infrared spectra were collected on a Nicolet iN10 Micro-IR spectrometer with an electrochemical IR cell using an ATR configuration under reaction conditions to monitor the evolution of interfacial species during electrolysis. The WE was prepared according to the "preparation of WEs" section during the testing process, and an Ag/AgCl electrode and a carbon rod were used as RE and CE, respectively. A CO_2-saturated electrolyte containing 0.5 M $KHCO_3$ and 0.05 M $KClO_4$ was used for CO_2RR to ethanol. The background spectrum was obtained at the open circuit potential before each measurement. Then, absorption spectra at different potentials with a spectral resolution of 4 cm^{-1} were collected. In the spectrum, a negative peak indicates the production or increase of a substance or functional group. The spectrum was collected after 2 min for each potential. The corresponding current responses recorded during the *in situ* ATR-FTIR measurements in different electrolytes have been added in Figure S43.

In situ *XAS spectroscopy*

The *in situ* Cr K-edge and Ag K-edge XAS spectroscopy were collected on the beamline BL11B of the SSRF. For the *in situ* XAS measurements, the WE was prepared according to the "preparation of WEs" section, and a Au wire and a saturated calomel electrode were used as the CE and the RE, respectively. An *in situ* electrochemical cell with polyimide film windows (XAFS-2, Gaossunion, China) was used, and the spectra were collected in fluorescence mode under potentiostatic conditions. The spectrum was collected after 5 min of stable operation for each potential. The corresponding current responses recorded during the *in situ* XAS measurements have been added in Figure S44. The data reductions of the experimental spectra to normalized XANES and Fourier-transformed radial distribution functions (RDFs) were performed through the standard XAS procedure.

Computational details

All the DFT calculations were performed using the Vienna Ab-initio Simulation Package (VASP). The exchange-correlation effects were described by the Perdew-Burke-Ernzerhof (PBE) functional within the generalized gradient approximation (GGA) method.[49,50] The core-valence interactions were treated using the projected augmented wave (PAW) method.[51] The energy cutoff for plane wave expansions was set to 400 eV, and the $3 \times 3 \times 1$ Monkhorst-Pack grid k-points were employed to sample the Brillouin zone integration. Structural optimization was carried out with energy and force convergence criteria set to 1.0×10^{-4} eV and 0.05 eV $Å^{-1}$, respectively.

The Gibbs free energy change (ΔG) of the reaction steps was calculated by the computational hydrogen electrode (CHE) model:

$$\Delta G = \Delta E + \Delta ZPE - T\Delta S,$$

where ΔE is the electronic energy difference directly obtained from DFT calculations, ΔZPE is the zero-point energy difference, T is the room temperature (298.15 K), and ΔS is the entropy change. ZPE (zero-point energy) could be obtained after frequency calculation by[52]:

$$ZPE = \frac{1}{2}\sum h\nu.$$

And the TS (T is the temperature and S is the entropy) values of adsorbed species are calculated according to the vibrational frequencies[53]:

$$TS = k_B T\left[\sum_k \ln\left(\frac{1}{1 - e^{-h\nu/k_B T}}\right) + \sum_k \frac{h\nu}{k_B T}\frac{1}{(e^{h\nu/k_B T} - 1)} + 1\right],$$

where k_B is the Boltzmann constant, h is the Planck constant, and ν stands for vibrational frequency.

AIMD simulations were performed using the freely available CP2K/Quickstep package. The PBE density functional with the Grimme D3 dispersion correction was used.[49,50] The 2s, 2p electrons of C, N, and O; the 3s, 3p electrons of P and Cl; and 4s and 3d electrons of Cr were treated as valence, and the rest of the core electrons were represented by Goedecker-Teter-Hutter (GTH) pseudopotentials.[54] The Gaussian basis set was double-ζ with one set of polarization functions (DZVP-MOLOPT-SR-GTH),[55] and the plane wave cutoff was set to 400 Ry. AIMD simulations were run with the constant-volume and constant-temperature ensemble by the CP2K package. The temperature was set to 300 K, and the time step was set to 0.5 fs. A nose-hoover thermostat was applied for temperature controlling. AIMD trajectories of about 80 ps were generated to compute the density profiles of O and H.

RESOURCE AVAILABILITY

Lead contact

Requests for further information and resources should be directed to and will be fulfilled by the lead contact, Qing Li (qing_li@hust.edu.cn).

Materials availability

This study did not generate any new, unique reagents.

Data and code availability

All data supporting the findings in this study are available within the paper and the supplemental information.

ACKNOWLEDGMENTS

This work was financially supported by the National Natural Science Foundation of China (22379048, 22579057, U24A20499 and 22479056). The authors thank the Analytical and Testing Center of Huazhong University of Science and Technology (HUST) for carrying out the HR-TEM, ^{1}H NMR, and ATR-FTIR measurements. The authors also thank the SSRF for the use of BL11B (https://cstr.cn/31124.02.SSRF.BL11B) and for the assistance with the XAS measurements.

AUTHOR CONTRIBUTIONS

Q.L. and T.W. conceived the idea and designed the experiments. S.L. and J.H. performed the synthesis, the material characterizations, and the electrochemical experiments. J.L., Z.L., and S.W. recorded and analyzed XAS and Raman data. Y.Z. and S.L. established the model and carried out the DFT calculations. T.W., H.S., and Q.L. analyzed the mechanism. S.L., T.W., and Q.L. co-wrote the paper. All the authors discussed the results and commented on the manuscript.

DECLARATION OF INTERESTS

The authors declare no competing interests.

SUPPLEMENTAL INFORMATION

Supplemental information can be found online at https://doi.org/10.1016/j.chempr.2026.103078.

Received: December 2, 2025
Revised: March 19, 2026
Accepted: May 7, 2026

Please cite this article in press as: Liu et al., Interfacial hydrogen-bond network regulation enables selective CO_2 reduction to ethanol on copper-free electrocatalysts, Chem (2026), https://doi.org/10.1016/j.chempr.2026.103078

REFERENCES

1. Feldman, D.R., Collins, W.D., Gero, P.J., Torn, M.S., Mlawer, E.J., and Shippert, T.R. (2015). Observational determination of surface radiative forcing by CO2 from 2000 to 2010. Nature *519*, 339–343. https://doi.org/10.1038/nature14240.
2. Wang, G.X., Chen, J.X., Ding, Y.C., Cai, P.W., Yi, L.C., Li, Y., Tu, C.Y., Hou, Y., Wen, Z.H., and Dai, L.M. (2021). Electrocatalysis for CO2 conversion: from fundamentals to value-added products. Chem. Soc. Rev. *50*, 4993–5061. https://doi.org/10.1039/d0cs00071j.
3. Ding, J., Bin Yang, H.B., Ma, X.L., Liu, S., Liu, W., Mao, Q., Huang, Y.Q., Li, J., Zhang, T., and Liu, B. (2023). A tin-based tandem electrocatalyst for CO2 reduction to ethanol with 80% selectivity. Nat. Energy *8*, 1386–1394. https://doi.org/10.1038/s41560-023-01389-3.
4. Farrell, A.E., Plevin, R.J., Turner, B.T., Jones, A.D., O'Hare, M., and Kammen, D.M. (2006). Ethanol can contribute to energy and environmental goals. Science *311*, 506–508. https://doi.org/10.1126/science.1121416.
5. Wang, T., Duan, X.Y., Bai, R., Li, H.Y., Qin, C., Zhang, J., Duan, Z.Y., Chen, K.J., and Pan, F.P. (2024). Ni-Electrocatalytic CO2 Reduction Toward Ethanol. Adv. Mater. *36*, 2410125. https://doi.org/10.1002/adma.202410125.
6. Fan, L.Z., Li, F., Liu, T.Q., Huang, J.E., Miao, R.K., Yan, Y., Feng, S.H., Tai, C.W., Hung, S.F., Tsai, H.J., et al. (2025). Atomic-level Cu active sites enable energy-efficient CO2 electroreduction to multicarbon products in strong acid. Nat. Synth. *4*, 262–270. https://doi.org/10.1038/s44160-024-00689-0.
7. Wang, P.T., Yang, H., Tang, C., Wu, Y., Zheng, Y., Cheng, T., Davey, K., Huang, X.Q., and Qiao, S.Z. (2022). Boosting electrocatalytic CO2-to-ethanol production via asymmetric C-C coupling. Nat. Commun. *13*, 3754. https://doi.org/10.1038/s41467-022-31427-9.
8. Chen, X., Jia, S.Q., Zhai, J.X., Jiao, J.P., Dong, M.K., Xue, C., Deng, T., Cheng, H.L., Xia, Z.H., Chen, C.J., et al. (2024). Multivalent Cu sites synergistically adjust carbonaceous intermediates adsorption for electrocatalytic ethanol production. Nat. Commun. *15*, 7691. https://doi.org/10.1038/s41467-024-51928-z.
9. Sun, K.A., Xie, S.H., Guan, P., Zhuang, Z.W., Tan, X., Yan, W., Zhang, J.J., and Chen, C. (2025). A bioinspired electrocatalyst for CO2 electroreduction to ethanol via secondary-sphere synergy in Fe porphyrinic-based metal-organic frameworks. Energy Environ. Sci. *18*, 6823–6831. https://doi.org/10.1039/d5ee01388g.
10. Li, Z.Y., Li, X., Wang, R.Y., Campos Mata, A.C., Gerke, C.S., Xiang, S.T., Mathur, A., Zhang, L.Y., Lin, D.Z., Li, T.C., et al. (2025). Electro-activated indigos intensify ampere-level CO2 reduction to CO on silver catalysts. Nat. Commun. *16*, 3206. https://doi.org/10.1038/s41467-025-58593-w.
11. Hussain, J., Jónsson, H., and Skúlason, E. (2018). Calculations of Product Selectivity in Electrochemical CO2 Reduction. ACS Catal. *8*, 5240–5249. https://doi.org/10.1021/acscatal.7b03308.
12. Vázquez-Parga, D., Jurado, A., Roldan, A., and Viñes, F. (2023). A computational map of the probe CO molecule adsorption and dissociation on transition metal low Miller indices surfaces. Appl. Surf. Sci. *618*, 156581. https://doi.org/10.1016/j.apsusc.2023.156581.
13. Zhao, Z.H., Huang, J.R., Liao, P.Q., and Chen, X.M. (2023). Highly Efficient Electroreduction of CO2 to Ethanol via Asymmetric C-C Coupling by a Metal-Organic Framework with Heterodimetal Dual Sites. J. Am. Chem. Soc. *145*, 26783–26790. https://doi.org/10.1021/jacs.3c08974.
14. Ringe, S., Clark, E.L., Resasco, J., Walton, A., Seger, B., Bell, A.T., and Chan, K. (2019). Understanding cation effects in electrochemical CO2 reduction. Energy Environ. Sci. *12*, 3001–3014. https://doi.org/10.1039/c9ee01341e.
15. Ren, W.H., Xu, A.N., Chan, K.R., and Hu, X.L. (2022). A Cation Concentration Gradient Approach to Tune the Selectivity and Activity of CO2 Electroreduction. Angew. Chem. Int. Ed. *61*, e202214173. https://doi.org/10.1002/anie.202214173.
16. Lee, S.Y., Kim, J., Bak, G., Lee, E., Kim, D., Yoo, S., Kim, J., Yun, H., and Hwang, Y.J. (2023). Probing Cation Effects on *CO Intermediates from Electroreduction of CO2 through Operando Raman Spectroscopy. J. Am. Chem. Soc. *145*, 23068–23075. https://doi.org/10.1021/jacs.3c05799.
17. Gu, J., Liu, S., Ni, W.Y., Ren, W.H., Haussener, S., and Hu, X.L. (2022). Modulating electric field distribution by alkali cations for CO2 electroreduction in strongly acidic medium. Nat. Catal. *5*, 268–276. https://doi.org/10.1038/s41929-022-00761-y.
18. Yoo, J.M., Ingenmey, J., Salanne, M., and Lukatskaya, M.R. (2024). Anion Effect in Electrochemical CO2 Reduction: From Spectators to Orchestrators. J. Am. Chem. Soc. *146*, 31768–31777. https://doi.org/10.1021/jacs.4c10661.
19. Hofmeister, F. (1888). Zur Lehre von der Wirkung der Salze. Archiv f. experiment. Pathol. u. Pharmakol. *24*, 247–260. https://doi.org/10.1007/BF01918191.
20. Marcus, Y. (2009). Effect of Ions on the Structure of Water: Structure Making and Breaking. Chem. Rev. *109*, 1346–1370. https://doi.org/10.1021/cr8003828.
21. Zhang, H., Raciti, D., and Hall, A.S. (2025). Disordered interfacial H2O promotes electrochemical C–C coupling. Nat. Chem. *17*, 1161–1168. https://doi.org/10.1038/s41557-025-01859-z.
22. Zhu, L.C., Pan, Y.F., Hua, Z.Y., Liu, Y., and Zhang, X. (2024). Ionic Effect on the Microenvironment of Biomolecular Condensates. J. Am. Chem. Soc. *146*, 14307–14317. https://doi.org/10.1021/jacs.4c04036.
23. Sheng, D.W., Liu, X.X., Yang, Z., Zhang, M., Li, Y., Ren, P.P., Yan, X.R., Shen, Z.X., and Chao, D.L. (2024). Hydrogen Bond Network Regulation in Electrolyte Structure for Zn-based Aqueous Batteries. Adv. Funct. Mater. *34*, 2402014. https://doi.org/10.1002/adfm.202402014.
24. Wang, Z.Z., Chen, Y.Q., Sheng, B.W., Li, J.L., Yao, L., Yu, Y., Song, J., Yu, T.Q., Li, Y.X., Pan, H., et al. (2024). Air-Promoted Light-Driven Hydrogen Production from Bioethanol over Core/Shell Cr2O3@GaN Nanoarchitecture. Angew. Chem. Int. Ed. *63*, e202400011. https://doi.org/10.1002/anie.202400011.
25. Akel, S., Dillert, R., Balayeva, N.O., Boughaled, R., Koch, J., El Azzouzi, M., and Bahnemann, D.W. (2018). Ag/Ag2O as a Co-Catalyst in TiO2 Photocatalysis: Effect of the Co-Catalyst/Photocatalyst Mass Ratio. Catalysts *8*, 647. https://doi.org/10.3390/catal8120647.
26. Zhang, B.X., Wang, J.M., Liu, G.M., Weiss, C.M., Liu, D.Q., Chen, Y.P., Xia, L.X., Zhou, P., Gao, M.X., Liu, Y.F., et al. (2024). A strongly coupled Ru-CrOx cluster-cluster heterostructure for efficient alkaline hydrogen electrocatalysis. Nat. Catal. *7*, 441–451. https://doi.org/10.1038/s41929-024-01126-3.
27. Zhou, Y.X., Yao, Y.B., Zhao, R., Wang, X.X., Fu, Z.Z., Wang, D.W., Wang, H.Z., Zhao, L., Ni, W., Yang, Z.Y., et al. (2022). Stabilization of Cu+ via Strong Electronic Interaction for Selective and Stable CO2 Electroreduction. Angew. Chem. Int. Ed. *61*, e202205832. https://doi.org/10.1002/anie.202205832.
28. Qiu, M.J., Sun, P., Han, K., Pang, Z.J., Du, J., Li, J.L., Chen, J., Wang, Z.L., and Mai, W.J. (2023). Tailoring water structure with high-tetrahedral-entropy for antifreezing electrolytes and energy storage at-80 °C. Nat. Commun. *14*, 601. https://doi.org/10.1038/s41467-023-36198-5.
29. Marcus, Y. (2010). Effect of ions on the structure of water. Pure Appl. Chem. *82*, 1889–1899. https://doi.org/10.1351/pac-con-09-07-02.
30. Wang, Y.H., Zheng, S.S., Yang, W.M., Zhou, R.Y., He, Q.F., Radjenovic, P., Dong, J.C., Li, S.N., Zheng, J.X., Yang, Z.L., et al. (2021). In situ Raman spectroscopy reveals the structure and dissociation of interfacial water. Nature *600*, 81–85. https://doi.org/10.1038/s41586-021-04068-z.
31. Liang, X.C., Chen, X.F., Zhai, Z.X., Yu, T.Q., Yu, H.Y., Wang, H.Q., Meng, D.X., Peng, L., and Yin, S.B. (2024). Synergistic modulation of hydrogen bond network reconstruction and pH buffering of electrolyte enables highly reversible Zn anode. Chem. Eng. J. *493*, 152622. https://doi.org/10.1016/j.cej.2024.152622.

32. Mao, J.L., Liang, J.S., Li, Y.N., Liu, X., Ma, F., Liu, S.X., Ouyang, H., Cai, Z., Wang, T.Y., Zhao, Y.F., et al. (2025). Electrochemical Lithiation Regulates the Active Hydrogen Supply on Ru-Sn Nanowires for Hydrogen Evolution Toward the High-Performing Anion Exchange Membrane Water Electrolyzer. J. Am. Chem. Soc. *147*, 7711–7720. https://doi.org/10.1021/jacs.4c17373.
33. Zhao, R., Wang, Q., Yao, Y.C., Wang, R.Z., Zhao, L., Hu, Z.W., Kao, C.W., Chan, T.S., Li, W.H., Zheng, Q., et al. (2025). Pd single atoms guided proton transfer along an interfacial hydrogen bond network for efficient electrochemical hydrogenation. Sci. Adv. *11*, 1602. https://doi.org/10.1126/sciadv.adu1602.
34. Speight, J.G. (2005). Lange's Handbook of Chemistry, Sixteenth Edition (McGraw-Hill).
35. Firet, N.J., and Smith, W.A. (2016). Probing the Reaction Mechanism of CO2 Electroreduction over Ag Films via Operando Infrared Spectroscopy. ACS Catal. *7*, 606–612. https://doi.org/10.1021/acscatal.6b02382.
36. Chernyshova, I.V., Somasundaran, P., and Ponnurangam, S. (2018). On the origin of the elusive first intermediate of CO2 electroreduction. Proc. Natl. Acad. Sci. USA *115*, E9261–E9270. https://doi.org/10.1073/pnas.1802256115.
37. Seiferth, O., Wolter, K., Dillmann, B., Klivenyi, G., Freund, H.-J., Scarano, D., and Zecchina, A. (1999). IR investigations of CO2 adsorption on chromia surfaces: Cr2O3(0001)/Cr(110) versus polycrystalline α-Cr2O3. Surf. Sci. *421*, 176–190. https://doi.org/10.1016/S0039-6028(98)00857-7.
38. Yu, Y.Q., Lin, K., Zhou, X.G., Wang, H., Liu, S.L., and Ma, X.X. (2007). New C-H Stretching Vibrational Spectral Features in the Raman Spectra of Gaseous and Liquid Ethanol. J. Phys. Chem. C *111*, 8971–8978. https://doi.org/10.1021/jp0675781.
39. Pitsevich, G.A., Doroshenko, I.Yu., Pogorelov, V.E., Shablinskas, V., Balevichus, V., and Kozlovskaya, E.N. (2012). Nonempiric Anharmonic Computations of IR Spectra of Ethanol Conformers in B3LYP/cc-pVQZ Approximation (Stretch C-H Vibrations). Am. J. Chem. *2*, 218–227. https://doi.org/10.5923/j.chemistry.20120204.06.
40. Cai, Z.W., Liang, J., Li, Z.X., Yan, T.Y., Yang, C.X., Sun, S.J., Yue, M., Liu, X.W., Xie, T., Wang, Y., et al. (2024). Stabilizing NiFe sites by high-dispersity of nanosized and anionic Cr species toward durable seawater oxidation. Nat. Commun. *15*, 6654. https://doi.org/10.1038/s41467-024-51130-1.
41. Zhang, J.W., Zeng, G.M., Zhu, S.Q., Tao, H.L., Pan, Y., Lai, W.C., Bao, J., Lian, C., Su, D., Shao, M.H., et al. (2023). Steering CO2 electroreduction pathway toward ethanol via surface-bounded hydroxyl species-induced noncovalent interaction. Proc. Natl. Acad. Sci. USA *120*, e2218987120. https://doi.org/10.1073/pnas.2218987120.
42. Fu, H.Q., Liu, J.X., Bedford, N.M., Wang, Y., Sun, J.W., Zou, Y., Dong, M.Y., Wright, J., Diao, H., Liu, P.R., et al. (2022). Synergistic Cr2O3@Ag Heterostructure Enhanced Electrocatalytic CO2 Reduction to CO. Adv. Mater. *34*, 2202854. https://doi.org/10.1002/adma.202202854.
43. Cao, X., Qin, H., Zhang, J., Chen, X., and Jiao, L. (2024). Regulation of Oxide Pathway Mechanism for Sustainable Acidic Water Oxidation. J. Am. Chem. Soc. *146*, 32049–32058. https://doi.org/10.1021/jacs.4c12942.
44. Henckel, D.A., Counihan, M.J., Holmes, H.E., Chen, X.Y., Nwabara, U.O., Verma, S., Rodríguez-López, J., Kenis, P.J.A., and Gewirth, A.A. (2021). Potential Dependence of the Local pH in a CO2 Reduction Electrolyzer. ACS Catal. *11*, 255–263. https://doi.org/10.1021/acscatal.0c04297.
45. Qin, Y.T., Zhan, G.M., Tang, C., Yang, D., Wang, X.B., Yang, J.H., Mao, C.L., Hao, Z.T., Wang, S.Y., Qin, Y.X., et al. (2023). Homogeneous Vacancies-Enhanced Orbital Hybridization for Selective and Efficient CO2-to-CO Electrocatalysis. Nano Lett. *23*, 9227–9234. https://doi.org/10.1021/acs.nanolett.3c01905.
46. Montoya, J.H., Shi, C., Chan, K., and Nørskov, J.K. (2015). Theoretical Insights into a CO Dimerization Mechanism in CO2 Electroreduction. J. Phys. Chem. Lett. *6*, 2032–2037. https://doi.org/10.1021/acs.jpclett.5b00722.
47. Pérez-Gallent, E., Figueiredo, M.C., Calle-Vallejo, F., and Koper, M.T.M. (2017). Spectroscopic Observation of a Hydrogenated CO Dimer Intermediate During CO Reduction on Cu(100) Electrodes. Angew. Chem. Int. Ed. *56*, 3621–3624. https://doi.org/10.1002/anie.201700580.
48. Kim, Y., Park, S., Shin, S.-J., Choi, W., Min, B.K., Kim, H., Kim, W., and Hwang, Y.J. (2020). Time-resolved observation of C–C coupling intermediates on Cu electrodes for selective electrochemical CO2 reduction. Energy Environ. Sci. *13*, 4301–4311. https://doi.org/10.1039/D0EE01690J.
49. Perdew, J.P., Burke, K., and Ernzerhof, M. (1996). Generalized gradient approximation made simple. Phys. Rev. Lett. *77*, 3865–3868. https://doi.org/10.1103/PhysRevLett.77.3865.
50. Kresse, G., and Joubert, D. (1999). From ultrasoft pseudopotentials to the projector augmented-wave method. Phys. Rev., B *59*, 1758–1775. https://doi.org/10.1103/PhysRevB.59.1758.
51. Blöchl, P.E. (1994). Projector augmented-wave method. Phys. Rev., B *50*, 17953–17979. https://doi.org/10.1103/PhysRevB.50.17953.
52. Nørskov, J.K., Rossmeisl, J., Logadottir, A., Lindqvist, L., Kitchin, J.R., Bligaard, T., and Jónsson, H. (2004). Origin of the overpotential for oxygen reduction at a fuel-cell cathode. J. Phys. Chem. B *108*, 17886–17892. https://doi.org/10.1021/jp047349j.
53. Bendavid, L.I., and Carter, E.A. (2013). CO2 Adsorption on Cu2O(111): A DFT+U and DFT-D Study. J. Phys. Chem. C *117*, 26048–26059. https://doi.org/10.1021/jp407468t.
54. VandeVondele, J., and Hutter, J. (2007). Gaussian basis sets for accurate calculations on molecular systems in gas and condensed phases. J. Chem. Phys. *127*, 124105. https://doi.org/10.1063/1.2770708.
55. Goedecker, S., Teter, M., and Hutter, J. (1996). Separable dual-space Gaussian pseudopotentials. Phys. Rev., B *54*, 1703–1710. https://doi.org/10.1103/PhysRevB.54.1703.